

Dual-Phase Spinel MnCo_2O_4 and Spinel MnCo_2O_4 /Nanocarbon Hybrids for Electrocatalytic Oxygen Reduction and Evolution

Xiaoming Ge,^{†,‡} Yayuan Liu,^{†,‡,§} F. W. Thomas Goh,[†] T. S. Andy Hor,^{*,†,⊥} Yun Zong,[†] Peng Xiao,^{||} Zheng Zhang,[†] Suo Hon Lim,[†] Bing Li,[†] Xin Wang,^{||} and Zhaolin Liu^{*,†}

[†]Institute of Materials Research and Engineering, A*STAR (Agency for Science, Technology and Research), 3 Research Link, Singapore 117602, Singapore

[§]School of Materials Science and Engineering, Nanyang Technological University, Nanyang Avenue, Singapore 639798, Singapore

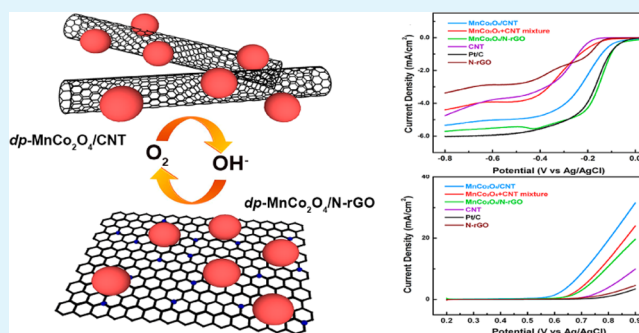
[⊥]Department of Chemistry, National University of Singapore, 3 Science Drive 3, Singapore 117543, Singapore

^{||}School of Chemical and Biomedical Engineering, Nanyang Technological University, 62 Nanyang Drive, Singapore 637459, Singapore

Supporting Information

ABSTRACT: Oxygen reduction reaction (ORR) and oxygen evolution reaction (OER) are essential reactions for energy-storage and -conversion devices relying on oxygen electrochemistry. High-performance, nonprecious metal-based hybrid catalysts are developed from postsynthesis integration of dual-phase spinel MnCo_2O_4 ($dp\text{-MnCo}_2\text{O}_4$) nanocrystals with nanocarbon materials, e.g., carbon nanotube (CNT) and nitrogen-doped reduced graphene oxide (N-rGO). The synergic covalent coupling between $dp\text{-MnCo}_2\text{O}_4$ and nanocarbons effectively enhances both the bifunctional ORR and OER activities of the spinel/nanocarbon hybrid catalysts. The $dp\text{-MnCo}_2\text{O}_4$ /N-rGO hybrid catalysts exhibited comparable ORR activity and superior OER activity compared to commercial 30 wt % platinum supported on carbon black (Pt/C). An electrically rechargeable zinc–air battery using $dp\text{-MnCo}_2\text{O}_4$ /CNT hybrid catalysts on the cathode was successfully operated for 64 discharge–charge cycles (or 768 h equivalent), significantly outperforming the Pt/C counterpart, which could only survive up to 108 h under similar conditions.

KEYWORDS: oxygen reduction reaction, oxygen evolution reaction, transition-metal oxide, spinel, nanocarbon, covalent coupling, metal–air battery



INTRODUCTION

The increasing global demand for energy, coupled with the depletion of fossil fuels and the associated detrimental environmental impact, has stimulated intense research on clean and sustainable energy-conversion and -storage systems.¹ Some energy-storage and -conversion devices relying on oxygen electrochemistry, such as rechargeable metal–air batteries and regenerative fuel cells, possess high theoretical specific energy and energy density and are cost-effective and environmentally benign.^{2,3}

Currently, the major bottleneck of devices based on oxygen electrochemistry lies in the lack of efficient and durable bifunctional catalysts for air cathodes, which are needed to overcome the sluggish kinetics of the oxygen reduction reaction (ORR) and oxygen evolution reaction (OER) during the discharge and charge stages, respectively.^{4,5} Although precious metal-based materials have shown desirable ORR catalytic activity,⁶ their large-scale application in reversible air electrodes is impeded by their high cost and scarcity, as well as the unsatisfactory OER activity.^{7,8} Nonprecious metal-based

efficient bifunctional catalysts are highly desirable but unfortunately have achieved little success in the current state of research and development.

Mixed-valent transition-metal oxides are potential candidates for bifunctional catalysts because of their high abundance, ease of preparation, and outstanding redox stability in aqueous alkaline solutions.^{9–12} Additionally, the variable valence states and structural flexibility of the spinel offer great opportunities to fine-tune their catalytic properties.^{13,14} Recent studies reported that the combination of oxides and nanocarbons such as graphene and carbon nanotube (CNT), which by themselves are good ORR catalysts,^{15–17} can improve the electrocatalytic activity and stability of the oxides by virtue of their excellent conductivity, large surface area, and high electrochemical stability.^{18,19} For example, directly anchored spinel/nanocarbon hybrid catalysts with high efficiency have

Received: May 1, 2014

Accepted: July 24, 2014

Published: July 24, 2014

been successfully produced from a two-step method or a one-pot synthesis. The resulting good catalytic performance could be attributed to the intimate electrical and chemical coupling between the oxide nanoparticles and nanocarbon backbones.^{20–25} The electrocatalytic performances of several cobalt-based spinel oxides such as Co_3O_4 ,²⁰ NiCo_2O_4 ,²¹ CuCo_2O_4 ,²⁴ $\text{Co}_3\text{O}_4/\text{MnCo}_2\text{O}_4$,²⁶ and $\text{MnCo}_2\text{O}_4/\text{CoMn}_2\text{O}_4$ ^{27–29} have been reported. Specifically, MnCo_2O_4 has been widely utilized in alkaline fuel cells³⁰ and solid oxide fuel cells,³¹ as well as for water treatment³² and glucose sensors.³³ Despite these efforts, studies on MnCo_2O_4 /nanocarbon bifunctional catalysts for ORR and OER are still limited.^{34–36} Significant performance gaps remain unfilled to furnish bifunctional catalytic activity on par with precious metal-based catalysts.

In this work, we report nonprecious metal-based spinel MnCo_2O_4 /nanocarbon hybrid catalysts with satisfactory bifunctional catalytic activities. MnCo_2O_4 nanocrystals of mixed cubic and tetragonal phases (hereafter *dp*- MnCo_2O_4), as confirmed by X-ray diffraction (XRD) and high-resolution transmission electron microscopy (HRTEM), were synthesized from a hydrothermal method followed by relevant heat treatments. To create the oxide/nanocarbon hybrids, we adopted an approach allowing both the *dp*- MnCo_2O_4 and nanocarbon to be tailored individually prior to integration, thus enabling delicate optimization of their structure and electrocatalytic performance. The covalent coupling phenomenon between *dp*- MnCo_2O_4 and nanocarbons, i.e., CNT or nitrogen-doped reduced graphene oxide (N-rGO), was revealed by X-ray photoelectron spectroscopy (XPS). The *dp*- MnCo_2O_4 /nanocarbon hybrids exhibited comparable ORR activity and superior OER activity compared to commercial 30 wt % carbon-supported platinum (Pt/C). Rechargeable metal–air battery results showed that the MnCo_2O_4 /nanocarbon hybrid catalysts greatly outperformed commercial Pt/C in terms of catalytic activity and durability. To the best of our knowledge, this is the first time that *dp*- MnCo_2O_4 /CNT and *dp*- MnCo_2O_4 /N-rGO hybrids are synthesized and demonstrated in the metal–air battery system as efficient ORR/OER bifunctional catalysts.

EXPERIMENTAL SECTION

2.1. Synthesis of MnCo_2O_4 Nanocrystals. In a typical synthesis, 698 mg of $\text{Co}(\text{NO}_3)_2 \cdot 6\text{H}_2\text{O}$ and 344 mg of $\text{Mn}(\text{NO}_3)_2 \cdot 6\text{H}_2\text{O}$ were dissolved in 55 mL of deionized (DI) water under gentle magnetic stirring to afford a homogeneous solution. Subsequently, 288 mg of NaOH was dissolved in 5 mL of DI water and added dropwise into the reaction mixture under vigorous stirring. The color of the solution first turned green and gradually evolved into greenish brown, brown, and finally dark brown when NaOH was added dropwise. After continuous stirring for 30 min, the reaction mixture was transferred into a 65 mL Teflon-lined stainless steel autoclave. The hydrothermal reaction was carried out at 160 °C for 10 h. The product was collected by centrifugation and washed four times with water and ethanol (volume ratio 1:1) before freeze-drying. Finally, the freeze-dried powder was calcined in air at 400 °C for 1 h.

2.2. Synthesis of *dp*- MnCo_2O_4 (80 wt %)/CNT and *dp*- MnCo_2O_4 (80 wt %)/N-rGO Hybrids. *dp*- MnCo_2O_4 /CNT hybrids with *dp*- MnCo_2O_4 contents of 60, 70, 80, and 90 wt % were prepared. In a typical example of *dp*- MnCo_2O_4 (80 wt %)/CNT, the calcined spinel was physically mixed with 20 wt % multiwalled CNT (Sigma-Aldrich). The mixture was subsequently heated under a nitrogen flow at 400 °C for 1 h and allowed to cool naturally to room temperature. Through this work, *dp*- MnCo_2O_4 /CNT stands for *dp*- MnCo_2O_4 (80 wt %)/CNT without further explanation. A 0.1 mg/mL graphene oxide (GO) solution was prepared by diluting the 1 wt % GO stock

solution (Mitsubishi Chemical Gas). The pH of the GO solution was adjusted to 8.0 using aqueous ammonia. Subsequently, an appropriate amount of the calcined spinel MnCo_2O_4 was added to the GO solution, making the weight ratio of MnCo_2O_4 to GO 4:1. Urea of 200 times the weight of GO was then added. The solution was sonicated for 1 h to afford a homogeneous mixture and transferred to a Teflon-lined stainless steel autoclave. The hydrothermal treatment was carried out at 170 °C for 12 h. The resulting hybrid catalyst was collected by centrifugation, washed four times with water and ethanol, and freeze-dried.

2.3. Material Characterization. Powder XRD patterns were recorded with a Bruker AXS D8 Advance diffractometer using nickel-filtered Cu K α radiation ($\lambda = 1.5406 \text{ \AA}$). Energy-dispersive X-ray (EDX) spectra were taken by a JEOL JSM5600 scanning electron microscope at an accelerating voltage of 20 kV. Transmission electron microscopy (TEM) images were taken by a JEOL JEM 2010F microscope at an accelerating voltage of 200 kV. The XPS spectra were obtained using a VG ESCALAB 200i-XL X-ray photoelectron spectrometer with monochromatic Al K α (1486.6 eV) radiation. Au 4f doublets were used as the reference for charge correction.

2.4. Cyclic Voltammetry (CV) and Rotating-Disk Electrode (RDE) Measurements. All of the electrochemical measurements were carried out via Autolab PGSTAT302N. A three-electrode cell configuration was employed with a working electrode of glassy carbon RDE of 5 mm diameter, a counter electrode of platinum foil, and a reference electrode of Ag/AgCl in 3 M KCl. The electrolyte used for all measurements was a 0.1 M KOH aqueous solution. To form a catalyst ink, 4 mg of catalyst and 13 μL of a 5 wt % Nafion solution were dispersed in 1 mL of a 2.5:1 (v/v) water/isopropanol mixed solvent for 30 min of sonication. An aliquot of 5 μL of the catalyst ink was applied to a glassy carbon RDE and allowed to dry in air, giving a catalyst loading of 0.1 mg/cm². An O₂-saturated electrolyte was prepared by purging O₂ (99.999% pure), and a flow of O₂ was maintained over the electrolyte during electrochemical measurements. In control experiments, CV measurements were performed in a N₂ (99.99% pure)-saturated electrolyte. For RDE measurements, the working electrode was scanned at a rate of 5 mV/s at various rotation rates (400, 625, 900, 1225, 1600, 2000, and 2500 rpm).

2.5. Zinc–Air Battery Tests. The air cathode was prepared by thoroughly mixing 50 wt % MnCo_2O_4 /CNT and 40 wt % carbon black in ethanol media for 1 h. Next, a 10 wt % Nafion solution was added to the slurry, and the mixture was further mixed for 1 h. The resulting catalyst slurry was coated on a carbon paper (10 BC, SGL Carbon) and dried at 70 °C for 1 h to achieve a catalyst loading of 1.0 mg/cm², with a working area of 0.5 cm². A polished zinc plate was used as the anode. The cathode and anode were assembled into a plastic cell filled with 25 mL of aqueous electrolyte consisting of 30 wt % KOH and 20 g/L ZnCl₂. The distance between the anode and cathode was 30 cm, and no separator was used. Battery testing and cycling experiments were performed at 25 °C using the recurrent galvanic pulse method (Maccor 4300), by discharging 5 mA for 4 h and charging 2.5 mA for 8 h. Pt/C was subjected to an identical route to serve as a benchmark.

RESULTS AND DISCUSSION

Typical synthesis methods of MnCo_2O_4 include sol–gel,³⁰ microwave heating,^{37,38} combustion,³⁹ polyol-based precursor route,⁴⁰ solvothermal,⁴¹ etc. These methods, however, generally yield submicron particles with poor uniformity. This work introduces a facile and cost-effective approach to producing large quantities of uniform MnCo_2O_4 nanocrystals. MnCo_2O_4 precursors were synthesized from a hydrothermal route using cobalt nitrate and manganese nitrate as the source materials and sodium hydroxide as the precipitating agent. The MnCo_2O_4 nanocrystals were obtained by a postsynthesis heat treatment of freeze-dried MnCo_2O_4 precursors at 400 °C for 1 h in air. EDX spectroscopy (Figure S1 in the Supporting Information, SI) confirms the Mn/Co ratio of 1:2.

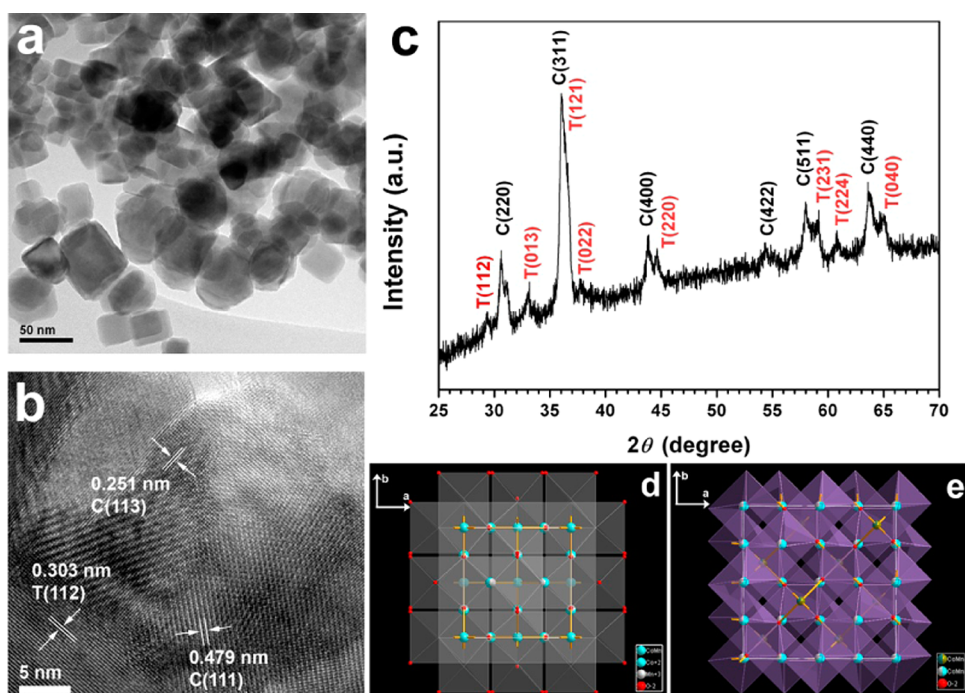


Figure 1. (a) TEM and (b) HRTEM images of the dp - MnCo_2O_4 nanocrystals after heat treatment. (c) XRD profile of dp - MnCo_2O_4 consisting of cubic $(\text{Mn}_{1/3}\text{Co}_{2/3})[\text{Mn}_{1/3}\text{Co}_{2/3}]_2\text{O}_4$ and tetragonal $(\text{Co, Mn})[\text{Mn, Co}]_2\text{O}_4$ and the structure visualization of (d) cubic $(\text{Mn}_{1/3}\text{Co}_{2/3})$ - $[\text{Mn}_{1/3}\text{Co}_{2/3}]_2\text{O}_4$ and (e) tetragonal $(\text{Co, Mn})[\text{Mn, Co}]_2\text{O}_4$ in the view of the c direction.

The TEM image shows that the particle sizes of MnCo_2O_4 nanocrystals are mostly in the range of 30–60 nm (Figure 1a), slightly larger than those in hybrid catalysts obtained from two-step methods or one-pot synthesis (average size <10 nm). This moderate particle size might be advantageous for the long-term performance of the catalysts because oxide particles that are too small are prone to high risk of agglomeration or leaching out from the material framework upon electrochemical cycling.⁴² Interestingly, the HRTEM image reveals the lattice fringes corresponding to the (111) and (113) planes of a cubic phase and the (112) plane of a tetragonal phase (Figure 1b). Obvious peak splittings are present in the powder XRD pattern of the calcined MnCo_2O_4 (Figure 1c). These two sets of diffraction reflections are indexed to be the cubic $(\text{Mn}_{1/3}\text{Co}_{2/3})$ - $[\text{Mn}_{1/3}\text{Co}_{2/3}]_2\text{O}_4$ phase ($Fd\bar{3}mZ$; ICSD 201314) and the less commonly observed tetragonal $(\text{Co, Mn})[\text{Mn, Co}]_2\text{O}_4$ phase ($I41/amdS$; ICSD 164369), where their structure visualizations are given in parts d and e of Figure 1, respectively, and the associated lattice settings are listed in Table S1 in the SI. The Rietveld refinement of the corresponding XRD pattern in Figure 1c indicates that dp - MnCo_2O_4 comprises 77 wt % of cubic $(\text{Mn}_{1/3}\text{Co}_{2/3})[\text{Mn}_{1/3}\text{Co}_{2/3}]_2\text{O}_4$ and 23 wt % of tetragonal $(\text{Co, Mn})[\text{Mn, Co}]_2\text{O}_4$ (Figure S2 in the SI).

The normal spinel structure, AB_2O_4 , has A cations occupying $1/8$ of the tetragonal sites and B cations occupying $1/2$ of the octahedral sites. In the inverse spinel structure $\text{B}[\text{AB}]_2\text{O}_4$, all of the A cations and half of the B cations occupy octahedral sites, while the other half of the B cations occupy tetrahedral sites. The two constituent phases of dp - MnCo_2O_4 , namely, $(\text{Mn}_{1/3}\text{Co}_{2/3})[\text{Mn}_{1/3}\text{Co}_{2/3}]_2\text{O}_4$ and $(\text{Co, Mn})[\text{Mn, Co}]_2\text{O}_4$, are intermediate spinel structures between the normal spinel structure and inverse spinel structure, with the formula of $(\text{A}_{1-x}\text{B}_x)[\text{A}_{x/2}\text{B}_{1-x/2}]_2\text{O}_4$. $(\text{Mn}_{1/3}\text{Co}_{2/3})[\text{Mn}_{1/3}\text{Co}_{2/3}]_2\text{O}_4$, i.e., $x = 2/3$ of $(\text{A}_{1-x}\text{B}_x)[\text{A}_{x/2}\text{B}_{1-x/2}]_2\text{O}_4$ adopts a fully random cation distribution of Co and Mn cations within the cubic-

close-packed oxygen anion lattices. The fully random Co and Mn distribution would result in fast exchange between Co and Mn cations and probably high transition metal–oxygen exchange rates, which could facilitate oxygen-related catalytic reactions such as ORR and OER. In the case of $(\text{Co, Mn})[\text{Mn, Co}]_2\text{O}_4$, nevertheless, Mn cations preferentially occupy the tetrahedral sites and displace some Co cations into the octahedral sites. By having an additional tetragonal spinel phase with Mn cations occupying some of the tetrahedral sites, the proportion of Co^{3+} cations occupying octahedral sites is increased compared to the homogeneous cubic $(\text{Mn}_{1/3}\text{Co}_{2/3})$ - $[\text{Mn}_{1/3}\text{Co}_{2/3}]_2\text{O}_4$. Because the surface Co^{3+} cations are known as active sites for OER in an alkaline solution,^{40,41} the tetragonal spinel structure is likely the cause of the uncompromised bifunctional activity of dp - MnCo_2O_4 (Figure S3 in the SI), which is observed to decrease with increasing Mn doping for Mn-rich $\text{Mn}_x\text{Co}_{3-x}\text{O}_4$ spinels.^{43,44}

Unlike noble-metal catalysts, oxide catalysts mediate electrochemical processes through surface redox reactions.^{5,45,46} Mixed-valence oxides are advantageous as bifunctional catalysts toward ORR and OER because the alternating valence states of cations can provide donor–acceptor chemisorption sites for the reversible adsorption/desorption of oxygen.¹³ Moreover, the electronic transfer processes can take place with relatively low activation energy between cations of different valences through the polaron hopping mechanism.⁴⁷ The $\text{Mn}^{4+}/\text{Mn}^{3+}$ redox couples located at the octahedral sites of the spinel structure were generally considered as the active sites for ORR and were more active than the Co species.^{41,46,48,49}

In this work, the electronic state of $\text{Mn}^{4+}/\text{Mn}^{3+}$ redox couples was tailored by the introduction of nanocarbon materials to establish the covalent interfacial Mn–O–C interactions (Mn–N–C interactions as well as dp - MnCo_2O_4 /N-rGO), where the electron sharing between C and O reduces the electron cloud density around Mn. Correspondingly, the

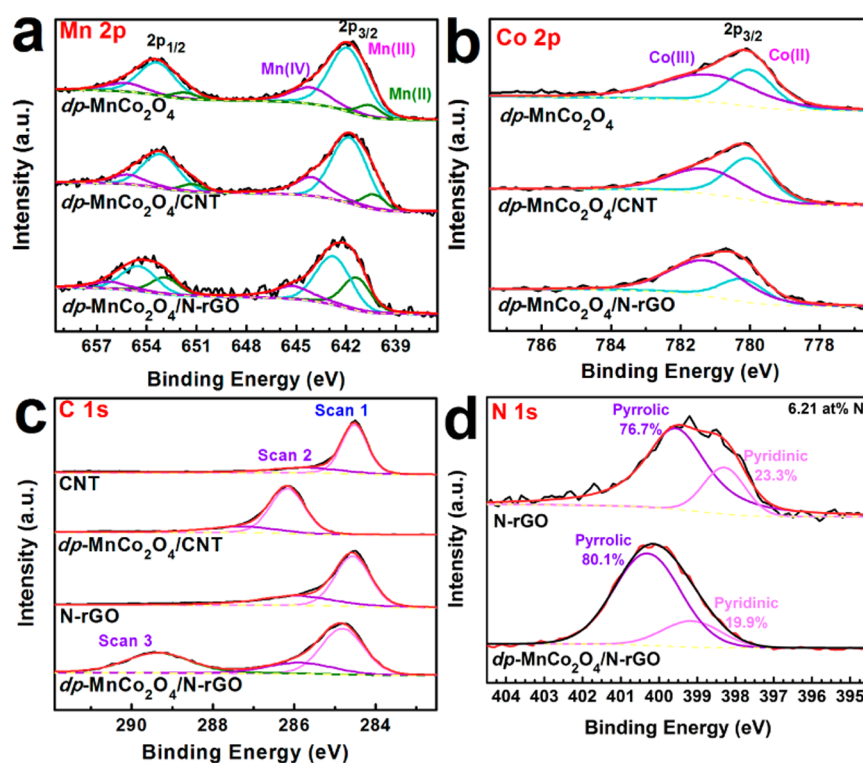


Figure 2. (a) Mn 2p high-resolution XPS spectra of $dp\text{-MnCo}_2\text{O}_4$, $dp\text{-MnCo}_2\text{O}_4/\text{N-rGO}$, and $dp\text{-MnCo}_2\text{O}_4/\text{CNT}$. (b) Co 2p high-resolution XPS spectra of $dp\text{-MnCo}_2\text{O}_4$, $dp\text{-MnCo}_2\text{O}_4/\text{N-rGO}$, and $dp\text{-MnCo}_2\text{O}_4/\text{CNT}$. (c) C 1s high-resolution XPS spectra of CNT, $dp\text{-MnCo}_2\text{O}_4/\text{CNT}$, N-rGO, and $dp\text{-MnCo}_2\text{O}_4/\text{N-rGO}$. (d) N 1s high-resolution XPS spectra of N-rGO and $dp\text{-MnCo}_2\text{O}_4/\text{N-rGO}$.

molecular orbital sharing between MnCo_2O_4 and nanocarbon shifts the $\text{Mn}^{4+}/\text{Mn}^{3+}$ redox couple to the Mn^{3+} end, thus resulting in improved ORR activities. To create spinel/nanocarbon hybrid catalysts, $dp\text{-MnCo}_2\text{O}_4$ nanocrystals were integrated with either CNT by calcination under an inert atmosphere or graphene via a second hydrothermal treatment in the presence of GO and urea. Urea in the hydrothermal treatment functioned as both the reducing agent and nitrogen source for the formation of N-rGO. The TEM images of various $dp\text{-MnCo}_2\text{O}_4$ /nanocarbon hybrid catalysts are given in Figures S5 and S6 in the SI.

XPS using Au 4f doublets as a reference for charge correction was employed to extensively investigate the surface elemental compositions and electronic configurations of the catalysts, as shown in Figure 2. Figure 2a confirms the positive shifts of the binding energy of Mn $2p_{3/2}$ peaks due to the covalent coupling effect between $dp\text{-MnCo}_2\text{O}_4$ and nanocarbons. The peak shifts of Mn $2p_{3/2}$ are +0.1 and +0.4 eV for $dp\text{-MnCo}_2\text{O}_4/\text{CNT}$ and $dp\text{-MnCo}_2\text{O}_4/\text{N-rGO}$, respectively (Table 1). The positive peak shift is also pronounced for Co cations, as reflected from Figure 2b. Notably, the surface Co/Mn ratio of the hybrid catalysts is much lower than the stoichiometric ratio of the bulk oxide, implying preferential accumulation of Mn species on the surfaces of $dp\text{-MnCo}_2\text{O}_4$ /nanocarbon hybrids. The high surface exposure of $\text{Mn}^{4+}/\text{Mn}^{3+}$ redox couples is favorable toward superior ORR performance.

Figure 2c shows the C 1s spectra of the different catalysts. Previous studies assigned the binding energy of the C–C and C–H bonds to be at 284.5–285 eV and had concluded that the existence of oxygenate groups can lead to a positive peak shift.⁵⁰ As shown in Figure 2c, the intensity of the peaks originated from C–O interactions (C 1s scan 2) is higher for $dp\text{-MnCo}_2\text{O}_4/\text{CNT}$ and $dp\text{-MnCo}_2\text{O}_4/\text{N-rGO}$ than for CNT and

Table 1. Summary of XPS Data for $dp\text{-MnCo}_2\text{O}_4$, $dp\text{-MnCo}_2\text{O}_4/\text{CNT}$, $dp\text{-MnCo}_2\text{O}_4/\text{N-rGO}$, CNT, and N-rGO

	Mn $2p_{3/2}$ (eV)	Mn ³⁺ /Mn ⁴⁺ pairs (% Mn)	Co $2p_{3/2}$ (eV)	Co/ Mn	C 1s scans 2 and 3 (% C)
$dp\text{-MnCo}_2\text{O}_4$	641.9	44.8	780.1	1.042	
$dp\text{-MnCo}_2\text{O}_4/\text{CNT}$	642.0	47.6	780.2	1.094	25.9
$dp\text{-MnCo}_2\text{O}_4/\text{N-rGO}$	642.3	45.1	780.7	1.085	53.1
CNT					23.9
N-rGO					33.1

N-rGO alone, indicating the existence of a stronger oxidized C environment due to the oxide–nanocarbon interactions. The coupling effect is especially pronounced for $dp\text{-MnCo}_2\text{O}_4/\text{N-rGO}$ because an additional C 1s peak (scan 3) was observed at 289.4 eV, probably as a result of the formation of C–O–transition metal or C–N–transition metal covalent bonds.⁵¹ Additionally, compared to N-rGO, the fraction of C atoms containing oxygenate functionalities is increased by 20% in $dp\text{-MnCo}_2\text{O}_4/\text{N-rGO}$, which could serve as further evidence for the strong covalent coupling between the spinel and nanocarbon.

More for the case of $dp\text{-MnCo}_2\text{O}_4/\text{N-rGO}$, the successful incorporation of nitrogen in graphene nanosheets during hydrothermal treatment was confirmed by XPS analysis (Figure 2d). The total nitrogen content is as high as 6.21%, and two types of N configurations, pyridinic N and pyrrolic N, are identified. Again, a positive shift of the binding energy of N 1s peaks is observed for $dp\text{-MnCo}_2\text{O}_4/\text{N-rGO}$ compared to that

of intrinsic N-rGO. This implies that the N species as well as the C species of N-rGO were involved in hybridization with dp - $MnCo_2O_4$ nanocrystals.

The electrocatalytic activities of the catalysts supported on glassy carbon RDEs were characterized by CV in O_2 - and N_2 -saturated 0.1 M aqueous KOH solutions (Figure 3a). CV

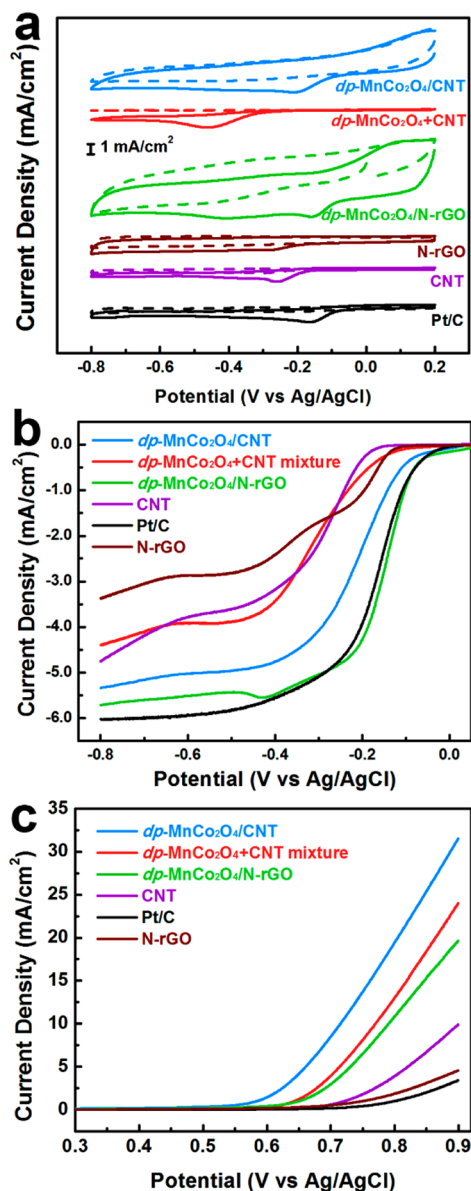


Figure 3. (a) CV curves (O_2 -saturated, solid line; N_2 -saturated, dashed line), (b) RDE oxygen reduction polarization curves and (c) RDE oxygen evolution polarization curves of dp - $MnCo_2O_4$, dp - $MnCo_2O_4$ /CNT hybrid, dp - $MnCo_2O_4$ /N-rGO hybrid, mechanically mixed dp - $MnCo_2O_4$ + CNT, CNT, N-rGO, and Pt/C in a 0.1 M KOH aqueous solution, with the rotating rate of 2000 rpm.

measurements with dp - $MnCo_2O_4$ /CNT and dp - $MnCo_2O_4$ /N-rGO hybrids reveal ORR onset potential and peak potential almost identical with those of commercial Pt/C (Table 2), indicating the salient ORR performance of the hybrid catalysts. Control experiments using N-rGO and CNT were conducted following the same catalyst preparation and testing route. Figure 3a shows that N-rGO and CNT alone exhibit certain

Table 2. Electrochemical Results of the dp - $MnCo_2O_4$ /Nanocarbon Catalysts and Pt/C^a

	ORR onset potential (V)	ORR current density at -0.8 V (mA/cm ²)	OER onset potential (V)	OER current density at $+0.8$ V (mA/cm ²)
dp - $MnCo_2O_4$ /CNT	-0.11	-5.33	0.53	19.45
dp - $MnCo_2O_4$ /N-rGO	-0.09	-5.71	0.59	10.85
Pt/C	-0.09	-6.01	0.67	1.02

^aThe rotating rate of RDE is 2000 rpm. The potential is versus Ag/AgCl (3 M KCl).

ORR catalytic activity but with much more negative ORR onset potentials and peak potentials.

RDE measurements were further employed to assess the ORR and OER kinetics of the catalysts (Figure 3b,c). RDE results show that the ORR/OER activities are optimized for the hybrid catalyst consisting of 80 wt % dp - $MnCo_2O_4$ and 20 wt % CNT (Figure S7 in the SI). As seen in Figure 3b, the ORR onset potentials of dp - $MnCo_2O_4$ /CNT and dp - $MnCo_2O_4$ /N-rGO hybrids are -0.11 and -0.09 V, respectively, which are essentially competitive with that of Pt/C (-0.09 V). The onset potential of dp - $MnCo_2O_4$ /N-rGO is consistent with those reported for $MnCo_2O_4$ /rGO and better than those for $MnCo_2O_4$ and Super P carbon black composite.^{21,35,41} As given in Figure 3b, the physical mixture of dp - $MnCo_2O_4$ and CNT shows improved ORR activity compared to each individual component alone. This suggests that the blended CNT helps to increase the electrical conductivity of dp - $MnCo_2O_4$, which by itself is a modest conductor.⁵² It is worth noting in Figure 3b that the ORR performance of the dp - $MnCo_2O_4$ /CNT hybrid is superior to that of the physically mixed counterpart, fully demonstrating the effectiveness of the spinel/nanocarbon hybridization strategy.

The leading edge of hybrid catalysts would result from the more efficiently established percolating network for electrical conduction, the more uniform and efficient distribution of nanocarbons and oxide catalysts, and the improved covalent coupling between oxide and nanocarbon. Most metal oxides generally have lower electrical conductivity than carbon-based materials, which may limit electron transport on their catalytically active sites. This issue becomes more prominent at high current density regions, where huge amounts of electrons flood into and out of the reaction sites on electrode surfaces during ORR and OER. Therefore, integration of metal oxides with nanocarbons promotes the formation of a conducting network, facilitating charge transfer during the electrochemical reactions at the oxide surfaces. The nanocarbon materials could also help to disperse oxide nanocrystals to prevent agglomeration, thereby increasing the accessible surface area of the catalysts.

The ORR polarization curves of dp - $MnCo_2O_4$ /N-rGO and Pt/C in the mixed kinetic- and diffusion-limiting region overlap with each other and show similar half-wave potential (Figure 3b), indicating the fast reaction kinetics of dp - $MnCo_2O_4$ /N-rGO in catalyzing ORR. In addition, a significant increase of the current density in the diffusion-limited region is observed for the hybrid catalysts. At -0.8 V, dp - $MnCo_2O_4$ /CNT, dp - $MnCo_2O_4$ /N-rGO, and Pt/C attain ORR current densities of 5.33, 5.71, and 6.01 mA/cm², respectively (Table 2). Note that

mechanically mixed $dp\text{-MnCo}_2\text{O}_4$ with nanocarbon could not afford strong hybrid coupling between the components, and therefore the electrocatalytic kinetics as well as the ORR current density of the $dp\text{-MnCo}_2\text{O}_4$ + CNT mixture were inferior to those of the $dp\text{-MnCo}_2\text{O}_4/\text{CNT}$ hybrid. This confirms the importance of covalent hybrid coupling for outstanding electrocatalytic performance.

To further understand the reaction mechanisms of the $dp\text{-MnCo}_2\text{O}_4/\text{nanocarbon}$ hybrids, Koutecky–Levich plots were generated at various electrode potentials. The least-squares-fitted slopes were used to calculate the number of electrons transferred (n) on the basis of the Koutecky–Levich equation:⁵³

$$\frac{1}{J} = \frac{1}{J_L} + \frac{1}{J_K} = \frac{1}{B\omega^{1/2}} + \frac{1}{J_K} \quad (1)$$

$$B = 0.2nFC_0(D_0)^{2/3}\nu^{-1/6} \quad (2)$$

$$J_K = nFkC_0 \quad (3)$$

where J is the measured current density, J_L is the diffusion-limiting current density, and J_K is the kinetic-limiting current density. ω is the angular velocity (rpm), n is the number of transferred electrons, F is the Faraday constant, C_0 is the bulk concentration of O_2 (1.21 mol/m³ in 0.1 M KOH),⁵⁴ D_0 is the diffusion coefficient of O_2 (1.87 × 10⁻⁹ m²/s in 0.1 M KOH),⁵⁵ ν is the kinematic viscosity of the electrolyte (10⁻⁶ m²/s in 0.1 M KOH),⁵⁴ and k is the electron-transfer rate constant. A potential region from -0.40 to -0.70 V of the voltammograms is selected to generate the Koutecky–Levich plots under rotating rates from 400 to 2500 rpm (Figure 4). The electron-transfer number (n) during ORR was calculated to be ~4.0, suggesting that the hybrid catalysts favor a desirable four-

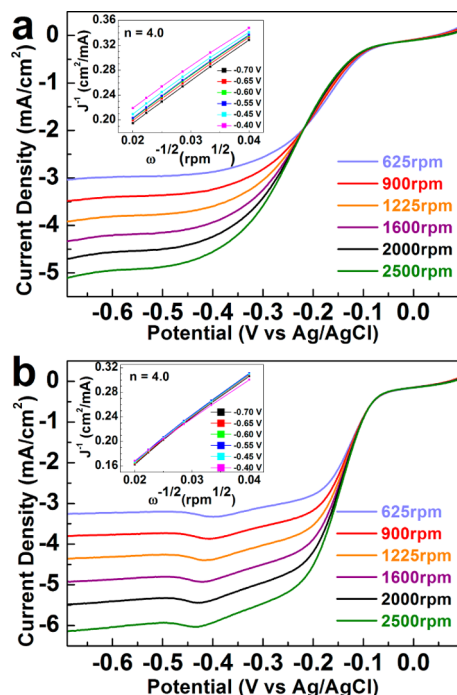


Figure 4. ORR polarization curves of (a) $dp\text{-MnCo}_2\text{O}_4/\text{CNT}$ hybrid and (b) $dp\text{-MnCo}_2\text{O}_4/\text{N-rGO}$ hybrid catalysts loaded on glassy carbon RDE in O_2 -saturated 0.1 M KOH at various rotation rates. The insets show the corresponding Koutecky–Levich plots at different potentials.

electron oxygen reduction pathway, similar to that of Pt/C. The Tafel plots indicate a significantly reduced Tafel slope for the hybrids in the low overpotential region compared to the bare $dp\text{-MnCo}_2\text{O}_4$ alone (Figure S9 in the SI). This is an indication of the enhanced ORR kinetics with integration of $dp\text{-MnCo}_2\text{O}_4$ with nanocarbons, consistent with the RDE results discussed above.

Besides the ORR activity, excellent OER activity is also crucial for bifunctional catalysts. The onset potentials of OER are 0.53 and 0.59 V for $dp\text{-MnCo}_2\text{O}_4/\text{CNT}$ and $dp\text{-MnCo}_2\text{O}_4/\text{N-rGO}$, respectively, both of which are significantly lower than the 0.67 V of Pt/C (Table 2). As can be observed from Figure 3c, the hybrid catalysts also afford much higher current density. The reduced OER onset potentials and higher current densities indicate that $dp\text{-MnCo}_2\text{O}_4/\text{nanocarbon}$ hybrids are better OER catalysts than Pt/C.

The bifunctional stability of $dp\text{-MnCo}_2\text{O}_4/\text{CNT}$ is evident from the unchanged morphologies of the catalyst before and after ORR/OER runs (cf. Figures S5c and S10 in the SI). The bifunctional activity and durability of the $dp\text{-MnCo}_2\text{O}_4/\text{nanocarbon}$ hybrid catalyst were further evaluated in a zinc–air battery prototype under realistic operating conditions. As shown in Figures 5 and S11 in the SI, superior battery

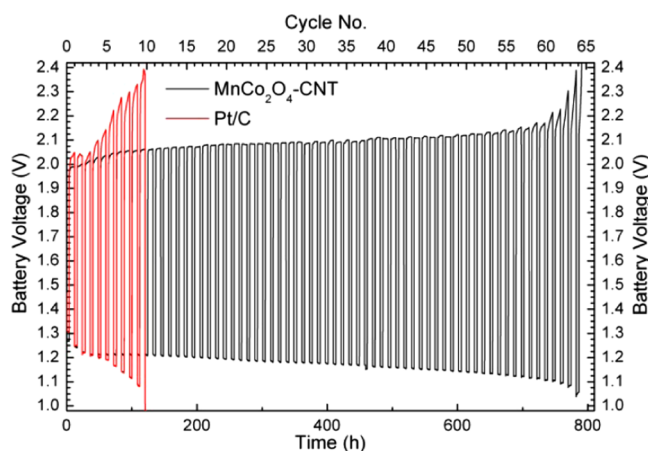


Figure 5. Cycling performance of rechargeable zinc–air batteries with $dp\text{-MnCo}_2\text{O}_4/\text{CNT}$ hybrid and Pt/C catalysts as the cathode. A cycle consists of a discharging stage under 10 mA/cm² for 4 h and a charging stage under 5 mA/cm² for 8 h.

performance is achieved by using $dp\text{-MnCo}_2\text{O}_4/\text{CNT}$ hybrid catalysts in the air cathode, which sustained 64 discharge–charge cycles (or 768 h equivalent) with degradation rates of only 0.08 and 0.13 mV/h for the discharging and charging stages, respectively. In comparison, the battery prototype with Pt/C catalysts was limited by merely 9 cycles (or 108 h equivalent), in which the degradation rate was as high as 3 mV/h. The striking contrast between $dp\text{-MnCo}_2\text{O}_4/\text{CNT}$ and Pt/C catalysts in the long-term battery test evidently demonstrates the high efficiency and durability of the $dp\text{-MnCo}_2\text{O}_4/\text{nanocarbon}$ hybrids. This study casts light on the design rationale of efficient and durable bifunctional catalysts that are low-cost and scalable for reversible electrochemical energy-storage and -conversion devices such as rechargeable metal–air batteries and regenerative fuel cells.

CONCLUSIONS

Spinel MnCo_2O_4 nanocrystals with mixed cubic and tetragonal phases ($dp\text{-MnCo}_2\text{O}_4$) were successfully synthesized from a facile hydrothermal route followed by appropriate thermal treatment. Subsequent integration of $dp\text{-MnCo}_2\text{O}_4$ with nanocarbon materials (N-rGO and CNT) created efficient ORR/OER bifunctional catalysts with comparable ORR activity and superior OER activity with regard to a commercial Pt/C. The synergic covalent coupling phenomena between $dp\text{-MnCo}_2\text{O}_4$ and nanocarbons were evident according to the binding energy shifts of Co, Mn, C, and N in the circumstances of with and without spinel/nanocarbon integration. The overall activity and durability of the hybrid catalysts outperformed Pt/C in electrically rechargeable metal–air batteries, whereby the prototype using the $dp\text{-MnCo}_2\text{O}_4/\text{CNT}$ hybrid performed stably over 64 discharge–charge cycles (or 768 h equivalent), compared to the Pt/C counterpart, which could only survive up to 108 h under similar conditions.

ASSOCIATED CONTENT

Supporting Information

XRD, EDX, TEM, and electrochemical results. This material is available free of charge via the Internet at <http://pubs.acs.org>.

AUTHOR INFORMATION

Corresponding Authors

*E-mail: andyhor@imre.a-star.edu.sg.

*E-mail: zl-liu@imre.a-star.edu.sg.

Author Contributions

[‡]These authors contributed equally.

Notes

The authors declare no competing financial interest.

ACKNOWLEDGMENTS

This research was supported by the Advanced Energy Storage Research Programme (Grants IMRE/12-2P0503 and IMRE/12-2P0504), Institute of Materials Research and Engineering (IMRE) of the Agency for Science, Technology and Research (A*STAR), Singapore, and the Industrial Orientation Programme of Nanyang Technological University, Singapore. The authors thank June Ong Lay Ting (IMRE) for her help in XPS characterization. The authors are grateful to Guojun Du for TEM.

REFERENCES

- (1) Arico, A. S.; Bruce, P.; Scrosati, B.; Tarascon, J. M.; van Schalkwijk, W. Nanostructured Materials for Advanced Energy Conversion and Storage Devices. *Nat. Mater.* **2005**, *4*, 366–377.
- (2) Cheng, F.; Chen, J. Metal–Air Batteries: from Oxygen Reduction Electrochemistry to Cathode Catalysts. *Chem. Soc. Rev.* **2012**, *41*, 2172–2192.
- (3) Chen, Z.; Yu, A.; Higgins, D.; Li, H.; Wang, H.; Chen, Z. Highly Active and Durable Core–Corona Structured Bifunctional Catalyst for Rechargeable Metal–Air Battery Application. *Nano Lett.* **2012**, *12*, 1946–1952.
- (4) Suntivich, J.; May, K. J.; Gasteiger, H. A.; Goodenough, J. B.; Shao-Horn, Y. A Perovskite Oxide Optimized for Oxygen Evolution Catalysis from Molecular Orbital Principles. *Science* **2011**, *334*, 1383–1385.
- (5) Suntivich, J.; Gasteiger, H. A.; Yabuuchi, N.; Nakanishi, H.; Goodenough, J. B.; Shao-Horn, Y. Design Principles for Oxygen-Reduction Activity on Perovskite Oxide Catalysts for Fuel Cells and Metal–Air Batteries. *Nat. Chem.* **2011**, *3*, 546–550.

- (6) Devadoss, A.; Sudhagar, P.; Das, S.; Lee, S. Y.; Terashima, C.; Nakata, K.; Fujishima, A.; Choi, W. B.; Kang, Y. S.; Paik, U. Synergistic Metal–Metal Oxide Nanoparticles Supported Electrocatalytic Graphene for Improved Photoelectrochemical Glucose Oxidation. *ACS Appl. Mater. Interfaces* **2014**, *6*, 4864–4871.

- (7) Bing, Y.; Liu, H.; Zhang, L.; Ghosh, D.; Zhang, J. Nanostructured Pt–Alloy Electrocatalysts for PEM Fuel Cell Oxygen Reduction Reaction. *Chem. Soc. Rev.* **2010**, *39*, 2184–2202.

- (8) Gorlin, Y.; Jaramillo, T. F. A Bifunctional Nonprecious Metal Catalyst for Oxygen Reduction and Water Oxidation. *J. Am. Chem. Soc.* **2010**, *132*, 13612–13614.

- (9) Cheng, F.; Shen, J.; Peng, B.; Pan, Y.; Tao, Z.; Chen, J. Rapid Room-Temperature Synthesis of Nanocrystalline Spinel as Oxygen Reduction and Evolution Electrocatalysts. *Nat. Chem.* **2011**, *3*, 79–84.

- (10) Suntivich, J.; Perry, E.; Gasteiger, H.; Shao-Horn, Y. The Influence of the Cation on the Oxygen Reduction and Evolution Activities of Oxide Surfaces in Alkaline Electrolyte. *Electrocatalysis* **2013**, *4*, 49–55.

- (11) Cheng, F.; Zhang, T.; Zhang, Y.; Du, J.; Han, X.; Chen, J. Enhancing Electrocatalytic Oxygen Reduction on MnO_2 with Vacancies. *Angew. Chem., Int. Ed.* **2013**, *52*, 2474–2477.

- (12) May, K. J.; Carlton, C. E.; Stoerzinger, K. A.; Risch, M.; Suntivich, J.; Lee, Y. L.; Grimaud, A.; Shao-Horn, Y. Influence of Oxygen Evolution during Water Oxidation on the Surface of Perovskite Oxide Catalysts. *J. Phys. Chem. Lett.* **2012**, *3*, 3264–3270.

- (13) Han, X.; Zhang, T.; Du, J.; Cheng, F.; Chen, J. Porous Calcium–Manganese Oxide Microspheres for Electrocatalytic Oxygen Reduction with High Activity. *Chem. Sci.* **2013**, *4*, 368–376.

- (14) Li, Y.; Hasin, P.; Wu, Y. $\text{Ni}(x)\text{Co}(3-x)\text{O}(4)$ Nanowire Arrays for Electrocatalytic Oxygen Evolution. *Adv. Mater.* **2010**, *22*, 1926–1929.

- (15) Fu, X. G.; Jin, J. T.; Liu, Y. R.; Wei, Z. Y.; Pan, F. P.; Zhang, J. Y. Efficient Oxygen Reduction Electrocatalyst Based on Edge-Nitrogen-Rich Graphene Nanoplatelets: Toward a Large-Scale Synthesis. *ACS Appl. Mater. Interfaces* **2014**, *6*, 3930–3936.

- (16) Liu, M. K.; Song, Y. F.; He, S. X.; Tjui, W. W.; Pan, J. S.; Xia, Y. Y.; Liu, T. X. Nitrogen-Doped Graphene Nanoribbons as Efficient Metal-Free Electrocatalysts for Oxygen Reduction. *ACS Appl. Mater. Interfaces* **2014**, *6*, 4214–4222.

- (17) Zhang, B.; Wen, Z.; Ci, S.; Mao, S.; Chen, J.; He, Z. Synthesizing Nitrogen-Doped Activated Carbon and Probing its Active Sites for Oxygen Reduction Reaction in Microbial Fuel Cells. *ACS Appl. Mater. Interfaces* **2014**, *6*, 7464–7470.

- (18) Wang, H.; Dai, H. Strongly Coupled Inorganic–Nano-Carbon Hybrid Materials for Energy Storage. *Chem. Soc. Rev.* **2013**, *42*, 3088–3113.

- (19) Bag, S.; Roy, K.; Gopinath, C. S.; Raj, C. R. Facile Single-Step Synthesis of Nitrogen-Doped Reduced Graphene Oxide– Mn_3O_4 Hybrid Functional Material for the Electrocatalytic Reduction of Oxygen. *ACS Appl. Mater. Interfaces* **2014**, *6*, 2691–2698.

- (20) Liang, Y.; Li, Y.; Wang, H.; Zhou, J.; Wang, J.; Regier, T.; Dai, H. Co_3O_4 Nanocrystals on Graphene as a Synergistic Catalyst for Oxygen Reduction Reaction. *Nat. Mater.* **2011**, *10*, 780–786.

- (21) Liang, Y.; Wang, H.; Zhou, J.; Li, Y.; Wang, J.; Regier, T.; Dai, H. Covalent Hybrid of Spinel Manganese–Cobalt Oxide and Graphene as Advanced Oxygen Reduction Electrocatalysts. *J. Am. Chem. Soc.* **2012**, *134*, 3517–3523.

- (22) Lee, D. U.; Kim, B. J.; Chen, Z. One-Pot Synthesis of a Mesoporous NiCo_2O_4 Nanoplatelet and Graphene Hybrid and its Oxygen Reduction and Evolution Activities as an Efficient Bifunctional Electrocatalyst. *J. Mater. Chem. A* **2013**, *1*, 4754–4762.

- (23) Li, Y.; Gong, M.; Liang, Y.; Feng, J.; Kim, J. E.; Wang, H.; Hong, G.; Zhang, B.; Dai, H. Advanced Zinc–Air Batteries Based on High-Performance Hybrid Electrocatalysts. *Nat. Commun.* **2013**, *4* (1805), 1–7.

- (24) Ning, R.; Tian, J. Q.; Asiri, A. M.; Qusti, A. H.; Al-Youbi, A. O.; Sun, X. P. Spinel CuCo_2O_4 Nanoparticles Supported on N-Doped Reduced Graphene Oxide: A Highly Active and Stable Hybrid

Electrocatalyst for the Oxygen Reduction Reaction. *Langmuir* **2013**, *29*, 13146–13151.

(25) Xiao, J.; Wan, L.; Wang, X.; Kuang, Q.; Dong, S.; Xiao, F.; Wang, S. Mesoporous Mn_3O_4 -CoO Core-Shell Spheres Wrapped by Carbon Nanotubes: A High Performance Catalyst for the Oxygen Reduction Reaction and CO Oxidation. *J. Mater. Chem. A* **2014**, *2*, 3794–3800.

(26) Wang, D. D.; Chen, X.; Evans, D. G.; Yang, W. S. Well-Dispersed $\text{Co}_3\text{O}_4/\text{Co}_2\text{MnO}_4$ Nanocomposites as a Synergistic Bifunctional Catalyst for Oxygen Reduction and Oxygen Evolution Reactions. *Nanoscale* **2013**, *5*, 5312–5315.

(27) Hu, L.; Zhong, H.; Zheng, X.; Huang, Y.; Zhang, P.; Chen, Q. CoMn_2O_4 Spinel Hierarchical Microspheres Assembled with Porous Nanosheets as Stable Anodes for Lithium-ion Batteries. *Sci. Rep.* **2012**, *2* (986), 1–8.

(28) Li, J.; Xiong, S.; Li, X.; Qian, Y. A facile route to Synthesize Multiporous MnCo_2O_4 and CoMn_2O_4 Spinel Quasi-Hollow Spheres with Improved Lithium Storage Properties. *Nanoscale* **2013**, *5*, 2045–2054.

(29) Zhou, L.; Zhao, D.; Lou, X. W. Double-Shelled CoMn_2O_4 Hollow Microcubes as High-Capacity Anodes for Lithium-Ion Batteries. *Adv. Mater.* **2012**, *24*, 745–748.

(30) Nissinen, T.; Valo, T.; Gasik, M.; Rantanen, J.; Lampinen, M. Microwave Synthesis of Catalyst Spinel MnCo_2O_4 for Alkaline Fuel Cell. *J. Power Sources* **2002**, *106*, 109–115.

(31) Liu, H. Y.; Zhu, X. F.; Cheng, M. J.; Cong, Y.; Yang, W. S. Electrochemical Performances of Spinel Oxides as Cathodes for Intermediate Temperature Solid Oxide Fuel Cells. *Int. J. Hydrogen Energy* **2013**, *38*, 1052–1057.

(32) Yang, W. S.; Hao, J. H.; Zhang, Z.; Lu, B. P.; Zhang, B. L.; Tang, J. L. Synthesis of Hierarchical MnCo_2O_4 Nanostructure Modified MnOOH Nanorods for Catalytic Degradation of Methylene Blue. *Catal. Commun.* **2014**, *46*, 174–178.

(33) Zhang, Y. Y.; Luo, L. Q.; Zhang, Z.; Ding, Y. P.; Liu, S.; Deng, D. M.; Zhao, H. B.; Chen, Y. G. Synthesis of MnCo_2O_4 Nanofibers by Electrospinning and Calcination: Application for a Highly Sensitive Non-Enzymatic Glucose Sensor. *J. Mater. Chem. B* **2014**, *2*, 529–535.

(34) Sa, Y. J.; Kwon, K.; Cheon, J. Y.; Kleitz, F.; Joo, S. H. Ordered Mesoporous Co_3O_4 Spinels as Stable, Bifunctional, Noble Metal-Free Oxygen Electrocatalysts. *J. Mater. Chem. A* **2013**, *1*, 9992–10001.

(35) Wang, H. L.; Yang, Y.; Liang, Y. Y.; Zheng, G. Y.; Li, Y. G.; Cui, Y.; Dai, H. J. Rechargeable $\text{Li}-\text{O}_2$ batteries with a Covalently Coupled MnCo_2O_4 -Graphene Hybrid as an Oxygen Cathode Catalyst. *Energy Environ. Sci.* **2012**, *5*, 7931–7935.

(36) Yuan, Y.; Bi, H. P.; He, G. Y.; Zhu, J. W.; Chen, H. Q. A Facile Hydrothermal Synthesis of a MnCo_2O_4 @Reduced Graphene Oxide Nanocomposite for Application in Supercapacitors. *Chem. Lett.* **2014**, *43*, 83–85.

(37) Liang, Q.; Chen, K.; Hou, W.; Yan, Q. CO Hydrogenation over Nanometer Spinel-Type Co/Mn Complex Oxides Prepared by Sol-Gel Method. *Appl. Catal., A* **1998**, *166*, 191–199.

(38) Nissinen, T. A.; Kiros, Y.; Gasik, M.; Leskela, M. MnCo_2O_4 Preparation by Microwave-Assisted Route Synthesis (MARS) and the Effect of Carbon Admixture. *Chem. Mater.* **2003**, *15*, 4974–4979.

(39) Das Sharma, A.; Mukhopadhyay, J.; Basu, R. N. Synthesis and Characterization of Nanocrystalline MnCo_2O_4 -Delta Spinel for Protective Coating Application in SOFC. *ECS Trans.* **2011**, *35*, 2509–2517.

(40) Liu, L.; Yang, Y. Z. Shape-Controlled Synthesis of Mn-Co Complex Oxide Nanostructures via a Polyol-Based Precursor Route and their Catalytic Properties. *Superlattices Microstruct.* **2013**, *54*, 26–38.

(41) Ma, S. C.; Sun, L. Q.; Cong, L. N.; Gao, X. G.; Yao, C.; Guo, X.; Tai, L. H.; Mei, P.; Zeng, Y. P.; Xie, H. M.; Wang, R. S. Multiporous MnCo_2O_4 Microspheres as an Efficient Bifunctional Catalyst for Nonaqueous $\text{Li}-\text{O}_2$ Batteries. *J. Phys. Chem. C* **2013**, *117*, 25890–25897.

(42) Yu, L.; Zhang, L.; Bin Wu, H.; Zhang, G. Q.; Lou, X. W. Controlled Synthesis of Hierarchical $\text{Co}_x\text{Mn}_{3-x}\text{O}_4$ Array Micro-

Nanostructures with Tunable Morphology and Composition as Integrated Electrodes for Lithium-Ion Batteries. *Energy Environ. Sci.* **2013**, *6*, 2664–2671.

(43) Rios, E.; Gautier, J. L.; Poillerat, G.; Chartier, P. Mixed Valency Spinel Oxides of Transition Metals and Electrocatalysis: Case of the $\text{Mn}_x\text{Co}_{3-x}\text{O}_4$ System. *Electrochim. Acta* **1998**, *44*, 1491–1497.

(44) Neburchilov, V.; Wang, H.; Martin, J. J.; Qu, W. A review on Air Cathodes for Zinc-Air Fuel Cells. *J. Power Sources* **2010**, *195*, 1271–1291.

(45) Bajdich, M.; Garcia-Mota, M.; Vojvodic, A.; Norskov, J. K.; Bell, A. T. Theoretical Investigation of the Activity of Cobalt Oxides for the Electrochemical Oxidation of Water. *J. Am. Chem. Soc.* **2013**, *135*, 13521–13530.

(46) El-Deab, M. S.; Ohsaka, T. Manganese Oxide Nanoparticles Electrodeposited on Platinum are Superior to Platinum for Oxygen Reduction. *Angew. Chem., Int. Ed.* **2006**, *45*, 5963–5966.

(47) Cheng, F.; Su, Y.; Liang, J.; Tao, Z.; Chen, J. MnO_2 -Based Nanostructures as Catalysts for Electrochemical Oxygen Reduction in Alkaline Media. *Chem. Mater.* **2009**, *22*, 898–905.

(48) De Koninck, M.; Marsan, B. $\text{Mn}_x\text{Cu}_{1-x}\text{Co}_2\text{O}_4$ Used as Bifunctional Electrocatalyst in Alkaline Medium. *Electrochim. Acta* **2008**, *53*, 7012–7021.

(49) Hamdani, M.; Singh, R.; Chartier, P. Co_3O_4 and Co-Based Spinel Oxides Bifunctional Oxygen Electrodes. *Int. J. Electrochem. Sci.* **2010**, *5*, 556–577.

(50) Yang, D.; Velamakanni, A.; Bozoklu, G.; Park, S.; Stoller, M.; Piner, R. D.; Stankovich, S.; Jung, I.; Field, D. A.; Ventrone, C. A.; Ruoff, R. S. Chemical Analysis of Graphene Oxide Films after Heat and Chemical Treatments by X-Ray Photoelectron and Micro-Raman Spectroscopy. *Carbon* **2009**, *47*, 145–152.

(51) Zhou, J. G.; Wang, J.; Fang, H. T.; Wu, C. X.; Cutler, J. N.; Sham, T. K. Nanoscale Chemical Imaging and Spectroscopy of Individual RuO_2 Coated Carbon Nanotubes. *Chem. Commun.* **2010**, *46*, 2778–2780.

(52) Wickham, D. G.; Croft, W. J. Crystallographic and Magnetic Properties of Several Spinels Containing Trivalent Ja-1044 Manganese. *J. Phys. Chem. Solids* **1958**, *7*, 351–360.

(53) Bard, A. J.; Faulkner, L. R. *Electrochemical Methods: Fundamentals and Applications*, 2nd ed.; Wiley: New York, 2011; pp 341–342.

(54) Goh, F. W. T.; Liu, Z.; Ge, X.; Zong, Y.; Du, G.; Hor, T. S. A. Ag Nanoparticle-Modified MnO_2 Nanorods Catalyst for Use as an Air Electrode in Zinc-air Battery. *Electrochim. Acta* **2013**, *114*, 598–604.

(55) Sharifi, T.; Hu, G.; Jia, X. E.; Wagberg, T. Formation of Active Sites for Oxygen Reduction Reactions by Transformation of Nitrogen Functionalities in Nitrogen-Doped Carbon Nanotubes. *ACS Nano* **2012**, *6*, 8904–8912.